RSC Advances

PAPER

View Article Online
View Journal | View Issue

Cite this: *RSC Adv.*, 2025, **15**, 31931

Photoelectrochemical water splitting using TiO_2/α-Fe_2O_3 heterojunction films produced by chemical vapour deposition

Abdullah M. Alotaibi, * Hussam M. Alzahrani, Saud M. Alosaimi, Abdullah M. Alqahtani, Mohammed A. Alhajji and Mohammed J. Alotaibi

This study reports the enhanced photoelectrochemical (PEC) performance of TiO_2/α-Fe_2O_3 heterostructure films fabricated *via* a sequential aerosol-assisted chemical vapour deposition (AACVD) of hematite at 450 °C, followed by atmospheric pressure CVD (APCVD) of anatase TiO_2 with controlled thickness. Structural analyses (XRD, Raman, XPS) confirmed phase purity and oxidation states, while UV-vis spectroscopy revealed a narrowed bandgap and extended visible light absorption for the heterostructures compared to pristine films. The optimized TiO_2/α-Fe_2O_3 (8 min) photoanode achieved a photocurrent density of 1.75 mA cm^{-2} at 1.23 V *vs.* RHE in 1.0 M NaOH under AM 1.5G illumination, representing a ~150% improvement over pure α-Fe_2O_3. Incident-photon-to-current efficiency (IPCE) reached 7.47% at 420 nm, with enhanced performance sustained across the visible range. Transient absorption spectroscopy (TAS) revealed prolonged charge carrier lifetimes, indicating suppressed electron–hole recombination. The heterojunction design also improved stability, maintaining performance for over 16 h compared to 6.5 h for hematite alone. These synergistic effects including narrowed bandgap, efficient charge separation, and enhanced light harvesting highlight the novelty of combining AACVD and APCVD in fabricating TiO_2/α-Fe_2O_3 heterostructures as durable, high-performance photoanodes for scalable solar hydrogen generation.

Received 15th July 2025
Accepted 24th August 2025

DOI: 10.1039/d5ra05064b

rsc.li/rsc-advances

1. Introduction

Photoelectrochemical water splitting is a promising approach for sustainable energy production.[1–5] Generating electricity from hydrogen is highly desirable since it serves as an eco-friendly energy carrier and helps reduce reliance on fossil fuels. However, conventional hydrogen production methods using oil, coal, and methane have detrimental environmental effects, especially regarding climate change, due to the significant carbon dioxide emissions they generate.[6–8] The application of photoanodes in water splitting has garnered significant interest since the work of Fujishima and Honda (1972).[9] Since that time, numerous studies have focused on enhancing PEC efficiency and improving catalyst stability.

TiO_2 naturally occurs in three crystalline forms, anatase, rutile, and brookite, and possesses a wide band gap (>3.0 eV), which limits its photo-absorption to the UV range.[10–12] However, hematite α-Fe_2O_3 features a lower bandgap (2.0–2.2 eV), enabling enhanced visible light absorption. Additionally, it is relatively non-toxic, chemically stable, cost-effective, and possesses a suitable valence band edge position.[13–18] These combined attributes establish hematite as one of the most promising metal oxides for water splitting.

Nevertheless, hematite has some notable limitations, one of which is its conduction band edge being positioned below the reversible hydrogen potential.[19] Additionally, the photogenerated holes in Fe_2O_3 exhibit limited efficiency in driving the water oxidation process, this is attributed to the short hole diffusion length in Fe_2O_3,[20] in contrast to the high penetration depth.[21] Several studies have employed hematite as a photoanode for oxygen evolution in water splitting; however, these materials require an external electrical bias to generate hydrogen.

It is important to note that, despite its theoretical potential, the actual efficiency of hematite for water splitting remains negligible in practice when compared to theoretical calculations (16.8%),[19,22] this is due to high charge recombination, limited hole diffusion length, and low electrical conductivity.

To enhance the efficiency of Fe_2O_3 in water splitting, various strategies have been employed, including doping it with different elements or combining α-Fe_2O_3 with other metal oxide semiconductors like TiO_2, Ta_2O_5, and WO_3.[19,23–27] In fact, the exploration of Fe_2O_3 for water splitting dates back quite a while, with the first paper on its use being published by Hardee and Bard.[28] They discovered that when Fe_2O_3 was placed on a Ti and Pt substrate, the photocurrent under 500 nm illumination in KCl was 0.8 V *versus* the saturated calomel electrode (V_{SCE}). In

King Abdulaziz City for Science and Technology (KACST), Hydrogen Technologies Institute, Saudi Arabia. E-mail: abalotaibi@kacst.gov.sa

the same year, another study by Quinn *et al.* reported that on Fe_2O_3 single crystals under 475 nm illumination in 0.5 M NaOH, the photocurrent density reached 1.57 mA cm^{-2} *versus* the reversible hydrogen electrode (V_{RHE}).[29]

However, as mentioned, the PEC performance of α-Fe_2O_3 can be enhanced through surface treatment and/or metal ion doping, which helps reduce electron–hole recombination[30] and increases donor density.[31] Surface treatment also leads to accelerated solar water oxidation.[32–34] It was found that heterojunction systems enhance PEC performance by facilitating efficient charge separation and reducing recombination of photogenerated electron–hole pairs. This leads to improved light absorption and higher photocurrent, boosting overall PEC water splitting efficiency. The study reports on WO_3/TiO_2 core/shell heterojunction photoanodes with a dendritic TiO_2 shell that significantly enhances photoelectrochemical water splitting performance.[35] The dendritic TiO_2 increases surface area and active sites, while the heterojunction improves charge separation and reduces recombination. This architecture leads to higher photocurrent density, better light absorption, and improved stability compared to individual WO_3 or TiO_2 electrodes, demonstrating the important role of dendritic TiO_2 in optimizing PEC efficiency. Another study focuses on surface engineering of CuO–Cu_2O heterojunction thin films to enhance their photoelectrochemical water splitting performance.[36] By optimizing the interface and surface properties, the heterojunction facilitates better charge separation and transport. As a result, the films exhibit increased photocurrent and improved stability during water splitting. In addition, the paper reports the fabrication of WO_3/$BiVO_4$ heterojunction photoanodes with nanostructured WO_3 to boost photoelectrochemical performance.[37] The nanostructuring enhances light absorption, charge separation, and interfacial charge transfer. Consequently, the photoanodes achieve higher photocurrent density and improved efficiency in water splitting.

In this paper, we present, for the first time, α-Fe_2O_3 deposited by AACVD on an FTO substrate at 450 °C, followed by anatase TiO_2 deposited as a second layer by APCVD and annealed at 500 °C to remove carbon contamination. This TiO_2/α-Fe_2O_3 layered approach enhanced both the water splitting efficiency and stability compared to pure α-Fe_2O_3 films. Additionally, TiO_2 films deposited using this method demonstrated excellent water splitting performance under sunlight. A pure Fe_2O_3 film, deposited *via* AACVD, proved effective for water splitting (0.8 mA cm^{-2} at 1.23 V *vs.* RHE) and remained stable for about 6.5 hours. A notable improvement in photocurrent density was observed for the heterojunction after coupling with TiO_2 (1.75 mA cm^{-2} at 1.23 V *vs.* RHE), which increased the stability to 16 hours. Transient absorption spectroscopy (TAS) was used to investigate charge carrier recombination dynamics and carrier lifetimes of the TiO_2/α-Fe_2O_3 films. A correlation between PEC efficiency and carrier lifetimes measured by TAS was identified.

2. Experimental section

2.1. General procedure

All chemicals used in these experiments were provided by Sigma-Aldrich Chemical Co. and were used without further purification. Deposition was carried out on a 10 × 20 mm^2 fluorine-doped tin oxide (FTO) glass. Before use, the FTO substrates were meticulously cleaned with acetone (99%), isopropanol (99.9%), and distilled water, and then dried in air.

2.2. Deposition conditions

[0.23 g, 0.905 mmol] of iron(II) acetylacetonate Fe[CH_3COCH=$C(O)CH_3$]$_2$ was dissolved in 60 mL of ethyl acetate in a glass bubbler. Aerosol-assisted chemical vapor deposition (AACVD) was then employed to deposit α-Fe_2O_3 thin films onto FTO glass substrate. The mist was transferred into the reactor using nitrogen (BOC Ltd, 99.99%) at a flow rate of 1.4 L min^{-1}, and deposition was carried out for 40 minutes at 450 °C. Afterward, the reactor was allowed to cool to room temperature under nitrogen before the films were removed and annealed at 500 °C in nitrogen at 2 L min^{-1} for 30 minutes to eliminate carbon contamination.

At this point, 40 mL of titanium(IV) isopropoxide [$Ti(OCH(CH_3)_2)_4$] was introduced into a glass bubbler. Atmospheric pressure chemical vapor deposition (APCVD) was used to deposit TiO_2 films on the FTO glass substrate, with α-Fe_2O_3 films forming as the second layer. Concurrently, titanium(IV) isopropoxide was heated in the bubbler to around 120 °C, and the vapor was transferred to the reactor *via* nitrogen (BOC Ltd, 99.99%) at a flow rate of 4 L min^{-1}. Deposition took place at 450 °C for TiO_2 and TiO_2/α-Fe_2O_3 films for different time intervals (4, 8, and 12 minutes) on the glass substrate, followed by annealing at 500 °C for 30 minutes (Fig. S1).

3. Photoelectrochemical performance (PEC)

PEC measurements were carried out using a 1 M NaOH electrolyte (Fluka, in ID water, pH = 13.6) in a three-electrode electrochemical cell under simulated sunlight (100 mW cm^{-2}, AM 1.5G). A platinum wire served as the counter electrode, and an Ag/AgCl electrode in saturated KCl was used as the reference. The photoelectrode was controlled by a potentiostat (Ivium Technology), with the reversible hydrogen electrode (RHE) potential given by the equation:

$$E_{RHE} = E_{AgCl} + 0.059pH + E^{\circ}_{AgCl},$$
$$\text{where } E^{\circ}_{AgCl} = 0.1976 \text{ V at } 25\ ^{\circ}C$$

The potential was scanned from −1.0 to 1.23 V at a rate of 50 mV s^{-1}, and sunlight was simulated using an Ivium CompactStat (IVIUM Technologies) Lamp at an intensity of 100 mW cm^{-2} (AM 1.5G). The illumination intensity was calibrated using a silicon reference cell and optical meter (Newport, Model 1918-R). Incident-photon-to-current efficiency (IPCE) measurements were performed with 1.0 M NaOH electrolyte and a 200 W Xe lamp at 1.23 V *vs.* RHE. IPCE values were calculated using the formula:

$$\text{IPCE}\% = \frac{12\,400 \times I_{SC}\ (\text{A cm}^{-2})}{\lambda\ (\text{nm}) \times P_{in}\ (\text{W cm}^{-2})} \times 100$$

where I_{SC} is the current density at 1.23 V *vs.* RHE, λ is the wavelength of the incident monochromatic light, and P_{in} is the light intensity at a specific wavelength. Mott–Schottky measurements were conducted in the dark at a 1 kHz frequency, using the same electrolyte as for IPCE.

The Applied Bias Photon-to-Current Efficiency (ABPE) was calculated according to the following equation:

$$\text{ABPE}\ (\%) = \frac{J \times (1.23 - V_b)}{P_{light}}$$

where J is the photocurrent density (mA cm^{-2}) measured by the electrochemical workstation, V_b is the applied bias *versus* RHE (V), and P_{light} is the incident light intensity under AM 1.5G (100 mW cm^{-2}) illumination.

4. Transient absorption spectroscopy (TAS)

Transient absorption measurements were conducted using a custom-built pump–probe setup. The monochromatic pump pulse was generated by a Q-switched laser system (InnoLAS, Picolo AOT MOPA, Picosecond Nd:YVO_4 Laser System), where the fundamental frequency was tripled to produce a 355 nm output, with the pulse energy adjusted to 300 μJ cm^{-2} using a reflective neutral medium filter. The broadband probe pulse, spanning from 420 nm to 1100 nm, was generated through a supercontinuum process by focusing a 1300 nm seed pulse onto a 3 mm *c*-cut sapphire crystal. This seed pulse was produced by an optical parametric amplifier (Light Conversion, TOPAS Prime) after being pumped by a commercial Ti:sapphire amplifier (Coherent Legend Elite Duo, 4.5 mJ, 3 kHz, 100 fs). The delay time between the pump and probe pulses was controlled by an electronic delay generator (Stanford Research System DG535) with a jitter of approximately 100 ps. The spot sizes of the laser pulses were determined by transmissivity through a 75 nm precision laser pinhole, with 20% for the pump and 50% for the probe, resulting in the pump pulse being over three times larger than the probe pulse. In the experiments, the pump and probe pulses were overlapped on the front surface of the samples. All measurements were performed at room temperature, and the samples were kept in a nitrogen-filled chamber.

5. Results and discussion

5.1. X-ray diffraction (XRD) and Raman spectroscopy

Powder X-ray diffraction (PXRD) was employed to examine the TiO_2/α-Fe_2O_3, pure α-Fe_2O_3, and pure TiO_2 films (Fig. 1a). The analysis revealed that the iron oxide was in the α-Fe_2O_3 phase, with diffraction peaks corresponding to the (012), (104), (110), (113), (024), (116), and (214) planes at 2θ values of 24.2°, 33.1°, 35.5°, 40.8°, 49.4°, 54.1°, and 62.5°, respectively. These findings

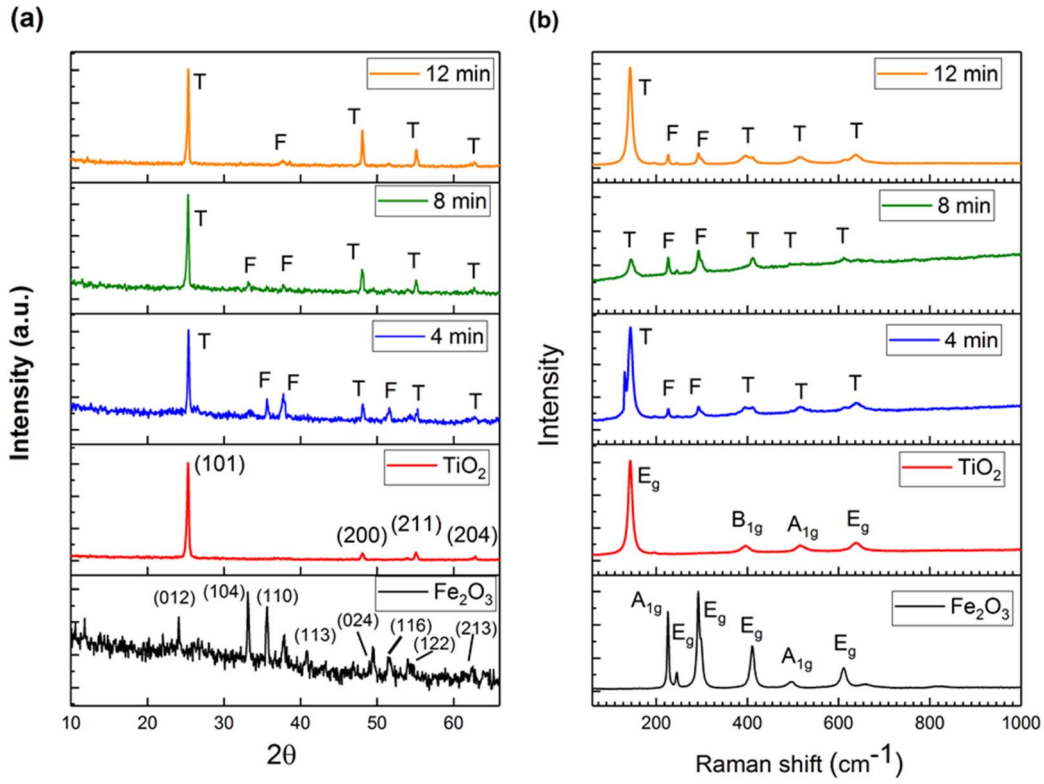

Fig. 1 (a) Shows the powder X-ray diffraction (PXRD) patterns of α-Fe_2O_3, TiO_2, and TiO_2/α-Fe_2O_3 layer films with varying TiO_2 thicknesses. (b) Displays the Raman spectra (recorded using a 633 nm laser wavelength) for all these films. The α-Fe_2O_3 film was deposited *via* AACVD at 450 °C on a glass substrate and annealed at 500 °C, while the pure TiO_2 and TiO_2 on α-Fe_2O_3 films were deposited using APCVD at 450 °C and annealed at 500 °C with different deposition durations (4, 8, and 12 minutes).

align well with the reference data for the α-Fe_2O_3 phase.[38,39] No peaks corresponding to other iron oxide phases were detected. The PXRD patterns for pure TiO_2 revealed a typical anatase phase, with diffraction peaks at (101), (112), (200), and (204) corresponding to 2θ values of 25.3°, 38.6°, 48.0°, 55.1°, and 62.8°, respectively.[40] The TiO_2/α-Fe_2O_3 films, with varying TiO_2 thicknesses, exhibited the anatase phase of TiO_2. However, for the films with a deposition time of 4, 8 and 12 minutes, a peak for α-Fe_2O_3 was observed, as the TiO_2 layer was thin enough to reveal the α-Fe_2O_3 peak. Fig. 1b presents the Raman spectra of TiO_2/α-Fe_2O_3, pure α-Fe_2O_3, and pure TiO_2 films. The Raman peaks for the Fe_2O_3 films appeared at 225 cm^{-1} (A_{1g}), 245 cm^{-1} (E_g), 292 cm^{-1} (E_g), 410 cm^{-1} (E_g), 502 cm^{-1} (A_{1g}), 497 cm^{-1} (E_g), and 612 cm^{-1} (E_g). The TiO_2 films in the anatase phase exhibited peaks at 141.5 cm^{-1} (E_g), 397 cm^{-1} (B_{1g}), 514 cm^{-1} (A_{1g}), and 635 cm^{-1} (E_g). The TiO_2/α-Fe_2O_3 films displayed peaks corresponding to both TiO_2 in the anatase phase and α-Fe_2O_3. These Raman spectra align with the XRD results, confirming the presence of iron oxide in the hematite phase and TiO_2 in the anatase phase.

5.2. UV-vis spectroscopy

The optical properties of TiO_2/Fe_2O_3 films, as well as pure Fe_2O_3 and TiO_2 films, were examined using UV-vis spectroscopy. Fig. 2a presents the absorption spectra of all the films. Pure TiO_2 exhibits absorption around 380 nm, as expected, while pure Fe_2O_3 and TiO_2/Fe_2O_3 films with deposition times of 4 and 8 minutes absorb near 600 nm, with absorption extending into the visible spectrum. The absorption of the TiO_2/Fe_2O_3 film (12 minutes) shows a slight shift towards the visible region, around 650 nm. Fig. 2a also shows the bandgaps of these films, which were calculated using Tauc plots.[41] The bandgaps of pure Fe_2O_3 and TiO_2 are approximately 1.95 eV and 3.2 eV, respectively. For the TiO_2/Fe_2O_3 films, the bandgaps are 2.1 eV, 2.1 eV, and 1.78 eV for deposition times of 4, 8, and 12 minutes, respectively.

Fig. 3 presents the UV-vis transmission spectra for all samples, displaying the characteristic interference fringes for TiO_2 and α-Fe_2O_3 based films. The transmission of TiO_2 films is approximately 72% for wavelengths between 380 and 780 nm, increasing to around 83% in the near-infrared region. In contrast, the transparency of hematite films deposited by AACVD is lower than that of TiO_2 films in the visible range, but fluctuates between 72% and 63% in the near-infrared. The transmission spectra of TiO_2/α-Fe_2O_3 films with a 12 minutes deposition time exhibit the lowest transparency in the visible range (500–760 nm), while the TiO_2/α-Fe_2O_3 films with a 4 minutes deposition time show a slight increase in transparency in the 700–2500 nm range compared to pure TiO_2 films.

5.3. X-ray photoelectron spectroscopy (XPS)

X-ray photoelectron spectroscopy (XPS) was employed to analyze the surface-level chemical states and valence band characteristics of all iron (Fe) and titanium (Ti) films. The $2p_{2/3}$ peaks corresponding to high-spin Fe^{2+} and Fe^{3+} ions displayed a notably broader profile compared to those observed in low-spin Fe^{2+} or metallic $Fe^{(0)}$.[42] Gupta and Sen have demonstrated that the broadening arises from three factors:

(1) The presence of unpaired 3d electrons in the photo-ionized Fe cation.

(2) Spin–orbit coupling involving the 2p core hole state.

(3) The incorporation of crystal field effects and electrostatic interactions.[43,44]

According to the study by Gupta and Sen, corroborated by additional research,[45,46] the Fe $2p_{3/2}$ peaks were analyzed using multiplet structure calculations. It was determined that the Fe $2p_{3/2}$ spectrum in α-Fe_2O_3 consists of four distinct components at 709.8, 710.7, 711.4, and 712.3 eV. Additionally, a satellite peak appears around 719 eV due to charge transfer processes and shake-up effects. Another peak, associated with surface structure, is observed at approximately 715 eV.[45]

The Fe spectrum was fitted using a Gaussian–Lorentzian function, revealing Fe 2p binding energies characteristic of Fe^{3+}.

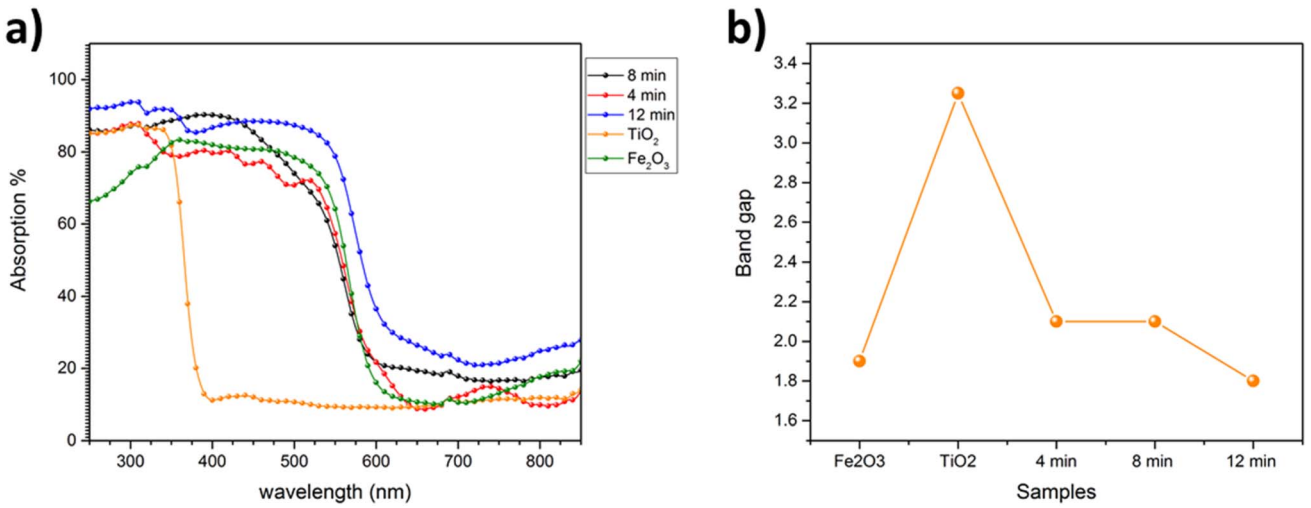

Fig. 2 (a) UV-vis absorption spectra of pure α-Fe_2O_3, TiO_2, and TiO_2/α-Fe_2O_3 films. (b) Displays the absorption spectra for all films, where pure TiO_2 absorbs around 380 nm and pure α-Fe_2O_3 film absorbs near 600 nm. The bandgaps, calculated using Tauc plots, are also shown in (b).

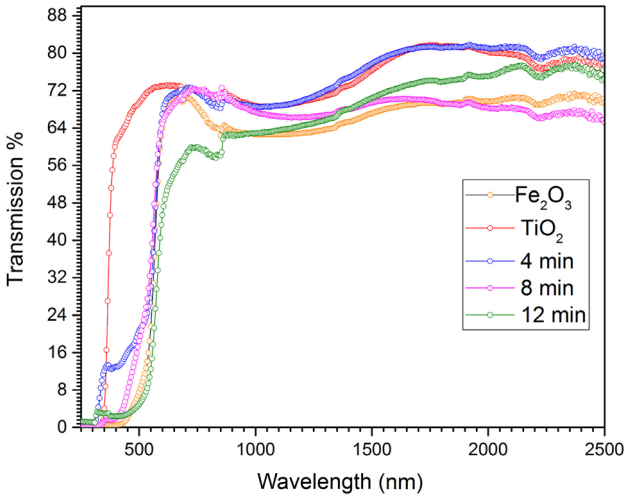

Fig. 3 Transmission spectra of α-Fe_2O_3, TiO_2 and TiO_2/α-Fe_2O_3 films deposited on glass substrate.

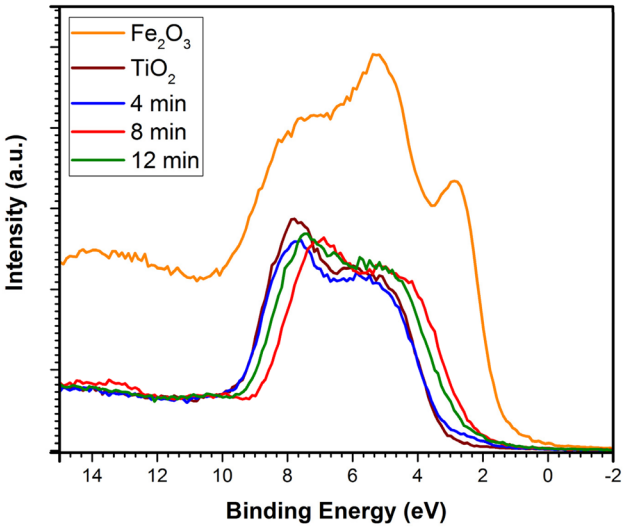

Fig. 5 Valence band XPS spectra of pure Fe_2O_3, TiO_2, and TiO_2/Fe_2O_3 films with deposition times of 4, 8, and 12 minutes. The VB spectra reveal a decrease in the band onset as the TiO_2 thickness increases.

The $2p_{3/2}$ peaks were centered at 709.2, 710.1, 710.6, 711.7, and 712.7 eV, with a pre-peak at 708.1 eV and a satellite peak at 719.1 eV. These results closely align with our samples, as illustrated in (Fig. 4a).

The XPS analysis of Ti 2p in pure TiO_2 and the α-Fe_2O_3 series revealed peaks at binding energies of 458.9 eV and 464.6 eV, corresponding to Ti–O bonds of Ti^{4+} within the TiO_2 lattice (Fig. 4b). The $2p_{3/2}$ peaks were more intense than the $2p_{1/2}$ peaks due to the greater degeneracy of $2p_{3/2}$ (four states) compared to $2p_{1/2}$ (two states) in spin–orbit (*j–j*) coupling. Additionally, no Ti^{3+} peak was detected in any of the samples.

Fig. 5 presents the XPS spectra of the valence band (VB) region for Fe_2O_3, TiO_2, and TiO_2/α-Fe_2O_3 films with varying TiO_2 thicknesses. While all VB spectra exhibit a main band spanning from 0 to approximately 10 eV, the VB spectrum of the α-Fe_2O_3 film also features three distinct bands at around 2.3, 4.8, and 7.5 eV, aligning well with the characteristic VB structure of α-Fe_2O_3.[46] The valence band (VB) spectra of TiO_2 and TiO_2/α-Fe_2O_3 films, deposited at different durations (4, 8, and 12 minutes), exhibit two primary peaks at approximately 4.2 and 7.5 eV. A slight shift in binding energy is observed as the TiO_2 film thickness increases compared to the pure TiO_2 film. The most significant distinction among the VB spectra of α-Fe_2O_3, TiO_2, and TiO_2/α-Fe_2O_3 samples is their intensity. The VB intensity of α-Fe_2O_3 is notably higher than that of TiO_2 or TiO_2/α-Fe_2O_3. This is attributed to the presence of Fe 3d (t_{2g} and e_g orbital symmetry) and O 2p hybridized states, along with the O 2p valence state. Additionally, the two lowest-energy peaks, at 2.3 and 4.8 eV, correspond to excitations of the $3e_g$ and $2t_{2g}$ orbitals, respectively. A third peak, located around 7.5 eV, is associated

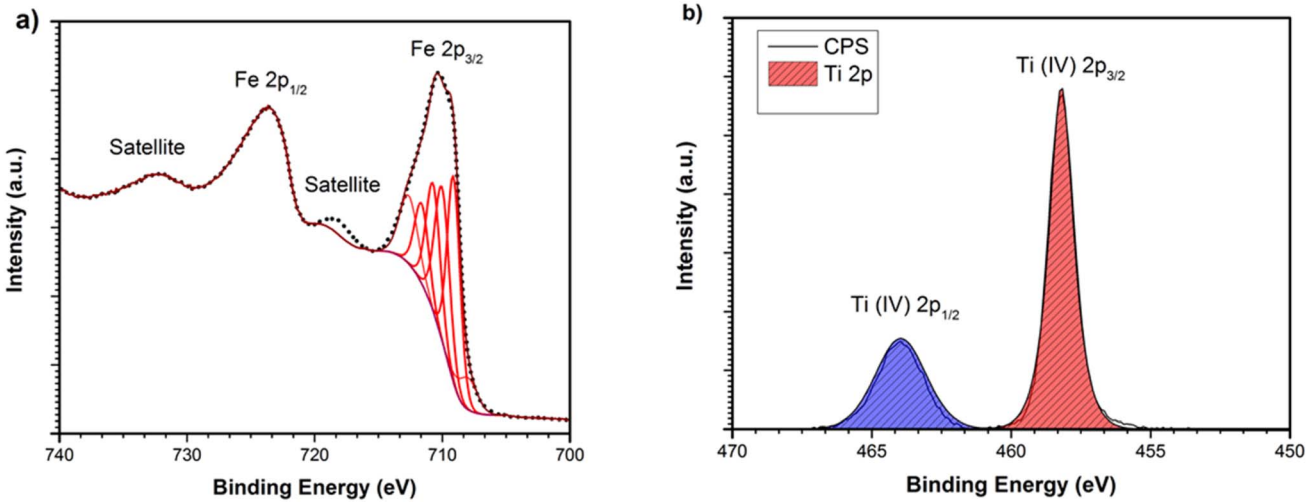

Fig. 4 Surface X-ray photoelectron spectra (XPS) of the Fe 2p region for: (a) α-Fe_2O_3, and (b) Ti, which remained in the +4 oxidation state across all films, with $2p_{3/2}$ peaks centered around 458.3 eV.

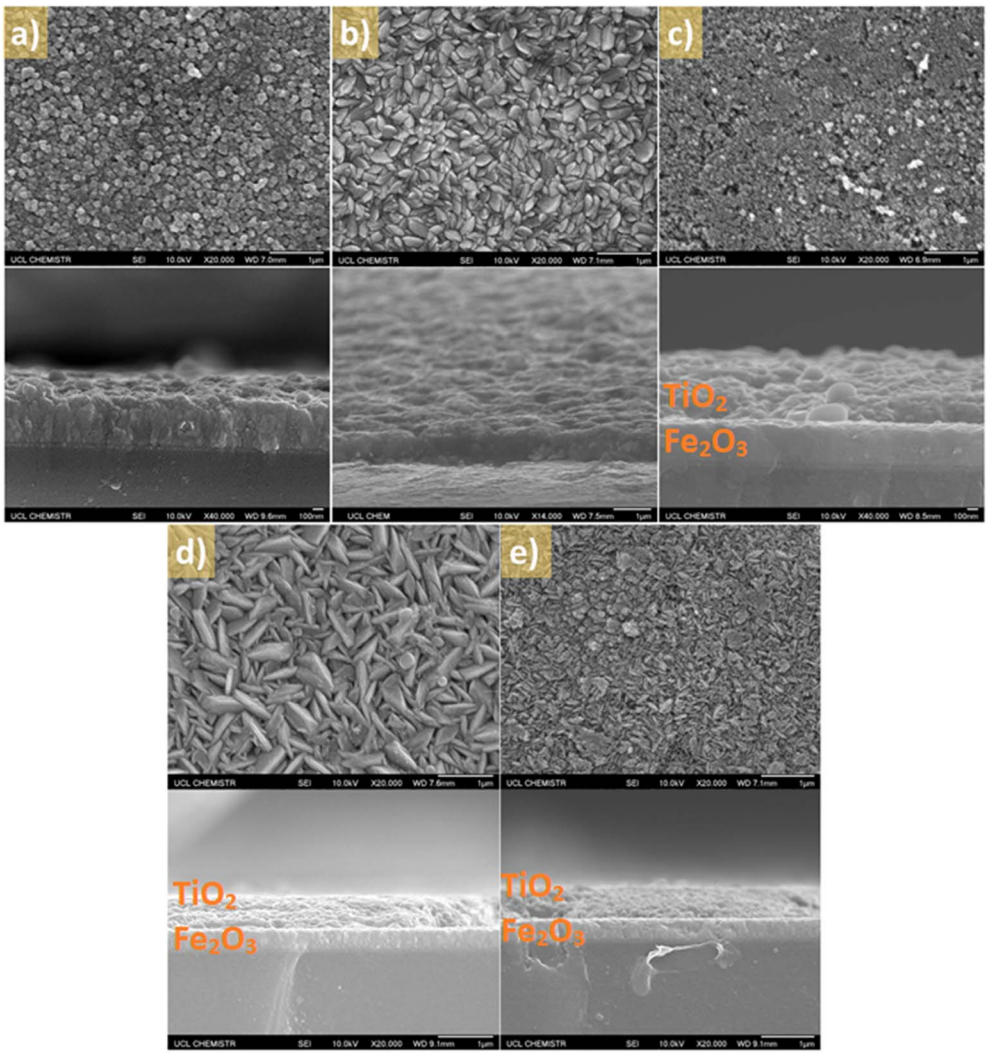

Fig. 6 SEM images of: (a) α-Fe_2O_3, (b) pure TiO_2, (c) TiO_2/α-Fe_2O_3 (4 min), (d) TiO_2/α-Fe_2O_3 (8 min), and (e) TiO_2/α-Fe_2O_3 (12 min) films grown by AACVD and APCVD on FTO at 450 °C and then annealed at 500 °C. The thicknesses are shown in side-view SEM images.

with the $2e_g$ orbital.[46] Additionally, the O 2p peaks overlap with the 4d orbitals, with the O 2p state appearing around 7.0 eV. Furthermore, the O 2p σ states overlap with the e_g peaks.[47] Conversely, the valence band (VB) spectra of TiO_2 films feature e_g and t_{2g} states at approximately 7.5 eV and 4.2 eV, respectively, arising from O 2p orbitals.[48]

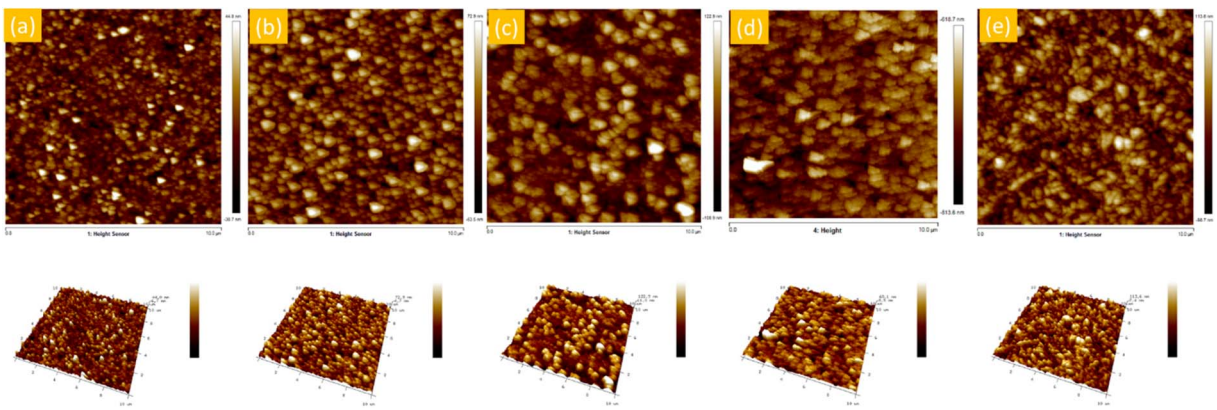

Fig. 7 2D (top) and 3D (bottom) surface images of: (a) α-Fe_2O_3, (b) TiO_2, and (c, d, and e) TiO_2/α-Fe_2O_3 films with deposition times of 4, 8, and 12 minutes, respectively, at a scale of 10 × 10 μm.

5.4. Scanning electron microscopy (SEM)

The morphology of Fe_2O_3, TiO_2, and TiO_2/α-Fe_2O_3 films was analyzed using SEM (Fig. 6). The α-Fe_2O_3 films exhibited approximately spherical particles with an average diameter of 100–200 nm (Fig. 6a), while the pure TiO_2 films featured densely packed particles ranging from 200 to 400 nm in diameter (Fig. 6b).

The morphology of the TiO_2/α-Fe_2O_3 films differed from that of the pure α-Fe_2O_3 and TiO_2 films. The TiO_2/α-Fe_2O_3 film with a deposition time of 4 minutes displayed particles with diameters ranging from 50 to 100 nm (Fig. 6c). The film deposited for 8 minutes had a similar morphology to pure TiO_2, consisting of densely packed particles approximately 500 nm wide (Fig. 6d). The TiO_2/α-Fe_2O_3 film with a deposition time of 12 minutes featured densely packed, needle-like particles, typically 200–400 nm in length (Fig. 6e).

Side-view micrographs revealed that the thickness of the pure α-Fe_2O_3 film on the substrate ranged from 368 to 422 nm (Fig. 6a), while the TiO_2 film was approximately 470 nm thick (Fig. 6b). The thicknesses of the TiO_2 layers in the TiO_2/α-Fe_2O_3 films with deposition times of 4, 8, and 12 minutes were around 438, 500, and 633 nm, respectively (Fig. 6c, d, and e).

5.5. Atomic force microscopy (AFM)

To further investigate the film morphology, AFM was employed to analyze the surface topography of all samples in this study (Fig. 7). AFM measurements were performed at a 10 × 10 μm scale. The resulting images reveal that the particles are similar, closely packed, pseudo-spherical grains. However, as shown in Fig. 6a, Fe_2O_3 appears to consist of smaller grains and has a flatter surface compared to the other samples. AFM images of TiO_2 and the TiO_2/α-Fe_2O_3 series showed particle aggregates, with varying surface roughness. This variation was quantified by measuring the RMS (root mean square) roughness of all samples at the 10 × 10 μm scale. The roughness of TiO_2 was 20.3 nm, nearly twice that of α-Fe_2O_3 (10.2 nm). The roughness values for the TiO_2/α-Fe_2O_3 (4 min) and TiO_2/α-Fe_2O_3 (12 min) samples were relatively similar, at 36.7 nm and 31.7 nm, respectively. In contrast, the TiO_2/α-Fe_2O_3 (8 min) sample exhibited a significantly lower surface roughness of about 19.8 nm. Additionally, the surface area of all samples was similar, with α-Fe_2O_3 having an area of 101 μm^2, and TiO_2, TiO_2/α-Fe_2O_3 (4 min, 8 min, and 12 min) having areas of 103, 104, 102, and 105 μm^2, respectively.

6. Photoelectrochemical (PEC) performances

Fig. 8 displays the current–voltage (I–V) curves for (a) TiO_2/α-Fe_2O_3 layers and pure α-Fe_2O_3, and (b) TiO_2 films, under both dark and simulated sunlight conditions (AM 1.5G, 100 mW cm^{-2}). As seen in Fig. 8a, the photocurrent of hematite in the dark increases sharply at a voltage of approximately 1.70 V_{RHE}. Under simulated sunlight, the onset potential shifts to around 0.4 V_{RHE}, with the photocurrent rising until about 1.4 V_{RHE}. The Fe_2O_3 photocurrent peaks at approximately 0.7 mA cm^{-2} at 1.23 V_{RHE}, where the RHE corresponds to the potential of the reversible oxygen electrode.

Fig. 8a also presents the photocurrent graphs for TiO_2/α-Fe_2O_3 films with varying TiO_2 thicknesses under sunlight conditions. It is evident that the TiO_2 layer, deposited by APCVD, not only enhances the photocurrent of α-Fe_2O_3 but also improves the onset potential. Specifically, the photocurrents of TiO_2/α-Fe_2O_3 (4 and 8 min) show onset potentials at 0.1 and 0.5 V_{RHE}, respectively, with currents increasing to approximately 1.2 and 1.75 mA cm^{-2} at 1.23 V_{RHE}. The sample with an 8-minute deposition time achieves a photocurrent of around 2.3 mA cm^{-2} at 1.45 V_{RHE}. However, for the thicker TiO_2 layer (12 min deposition time), the photocurrent decreased compared to pure

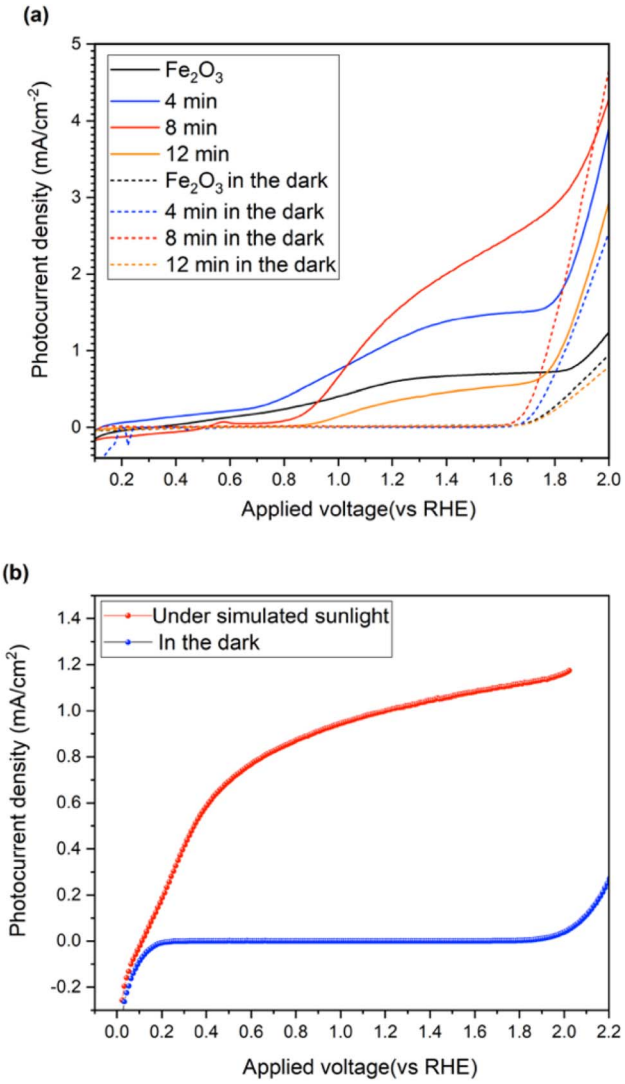

Fig. 8 PEC performance of (a) hematite and TiO_2/hematite films with varying deposition times (4, 8, and 12 minutes); (b) TiO_2 films. All films were deposited on FTO glass. Hematite was deposited using AACVD at 450 °C with Fe(II) acetylacetonate dissolved in ethyl acetate. TiO_2 films were prepared *via* APCVD using titanium isopropoxide at 450 °C, followed by a 1-hour annealing under nitrogen to eliminate carbon contamination. Water oxidation was tested in 1.0 M NaOH (pH 13.7) under both dark and AM 1.5G illumination (100 mW cm^{-2}).

Table 1 Comparing the photocurrents of some α-Fe_2O_3 heterojunction photoanodes obtained from the literature with our work

Photocathode	Electrolyte	Photocurrent density (mA cm^{-2})	References
TiO_2/Fe_2O_3 core/shell nanostructure	1 M KOH	0.91 mA cm^{-2} at 1.23 V *vs.* RHE	50
Fe_2O_3/g-C_3N_4 heterojunction	1 M KOH	1.02 mA cm^{-2} at 1.23 V *vs.* RHE	51
CQDs modified TiO_2/Sn–Fe_2O_{3-x} heterojunction	1 M KOH	1.47 mA cm^{-2} at 1.23 V *vs.* RHE	52
WO_3/Fe_2O_3 nanocomposite	0.5 M Na_2SO_4	2.34 mA cm^{-2} at 1.4 V *vs.* RHE	53
$BiVO_4/WO_3$/W heterojunction	0.1 M KH_2PO_4	2.01 mA cm^{-1-2} at 0.6 V (*vs.* Ag/AgCl)	54
α-Fe_2O_3/CuO	0.05 M Na_2SO_4	0.53 mA cm^{-2} at 1.0 V *vs.* RHE	55
ZnO/Fe_2O_3 core–shell nanowires	1 M NaOH	1.5 mA cm^{-2} at 0.6 V *vs.* Ag/AgCl	56
TiO_2/α-Fe_2O_3	1 M NaOH	1.7 mA cm^{-2} at 1.23 V *vs.* RHE	This work

hematite, reaching approximately 0.3 mA cm^{-2} at 1.2 V_{RHE}. For all samples, the *J–V* curves in the dark conditions increased up to 1.67 V_{RHE}.

The highest photocurrent recorded for Fe_2O_3 to date was reported by Michael Grätzel *et al.* in 2011, reaching approximately 2.3 mA cm^{-2} at 1.23 RHE.[15] Guo *et al.*[49] enhanced the performance of the hematite photoanode by doping hematite nanorod films with Ru, resulting in the best performance to date, achieving approximately 5.7 mA cm^{-2} at 1.23 RHE. The pure TiO_2 (with an 8-minute deposition time) was fabricated onto PEC photoanodes, and its performance was evaluated in 1.0 M NaOH under both dark and simulated sunlight (AM 1.5G, 100 mW cm^{-2}) conditions. As shown in Fig. 8b, the photocurrent density of this TiO_2 sample under sunlight conditions was approximately 1.0 mA cm^{-2} at 1.23 V_{RHE}, which is higher than previously reported for undoped TiO_2. Under dark conditions, the photocurrent of the same sample increased rapidly at around 1.9 V_{RHE}. However, an optimal TiO_2 thickness on α-Fe_2O_3 can enhance hole injection through surface contact with the solution, thereby reducing electron–hole recombination – a phenomenon confirmed by transient absorption spectroscopy (TAS) (see the TAS section). Although the optimized TiO_2/α-Fe_2O_3 heterojunction achieved a photocurrent density (1.75 mA cm^{-2} at 1.23 V *vs.* RHE) slightly lower than the record value reported for hematite nanostructures, the present work demonstrates a scalable, low-temperature AACVD–APCVD fabrication route that delivers competitive efficiency, significantly enhanced operational stability, and mechanistic insight *via* TAS into charge carrier dynamics. These combined advances highlight the practical potential of TiO_2/α-Fe_2O_3 photoanodes for durable, large-area solar hydrogen generation. However, Table 1 provides a comparison of photocurrents reported for various Fe_2O_3 photoanodes in previous studies with our TiO_2/α-Fe_2O_3 photoanode.

The positions of the valence and conduction band edges of TiO_2 and Fe_2O_3 films in contact with an electrolyte at pH 13.7, relative to the reversible hydrogen electrode (RHE) potential, were determined from the flat band measurements (Fig. 9). The band gaps of TiO_2 and Fe_2O_3 were found to be 3.2 eV and 1.95 eV, respectively. The conduction band of TiO_2 is positioned at 0.16 eV, while hematite shows a conduction band at 0.46 eV. Both of these conduction band edges are below the H_2O/H_2 electrochemical level for water reduction, meaning they cannot reduce H_2O without the application of an external bias (Fig. 9). Additionally, the conduction band of the Fe_2O_3 film is more positive than that of anatase TiO_2, which aligns with the photocurrent onset potential observed in Fig. 8. The valence band of the TiO_2 film lies significantly deeper than that of the Fe_2O_3 film and even falls below the water oxidation potential of 1.23 V *vs.* NHE, making it capable of oxidizing H_2O to O_2 (Fig. 9).

However, the heterogeneous system consisting of TiO_2 deposited on α-Fe_2O_3 thin film, which is itself on a FTO glass

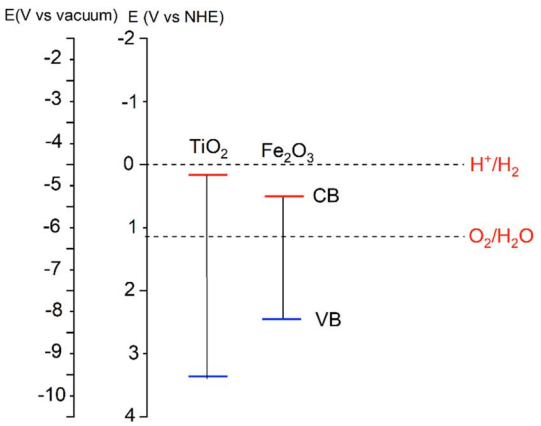

Fig. 9 Positions of the valence and conduction bands of TiO_2 and Fe_2O_3 thin films at pH = 13.7.

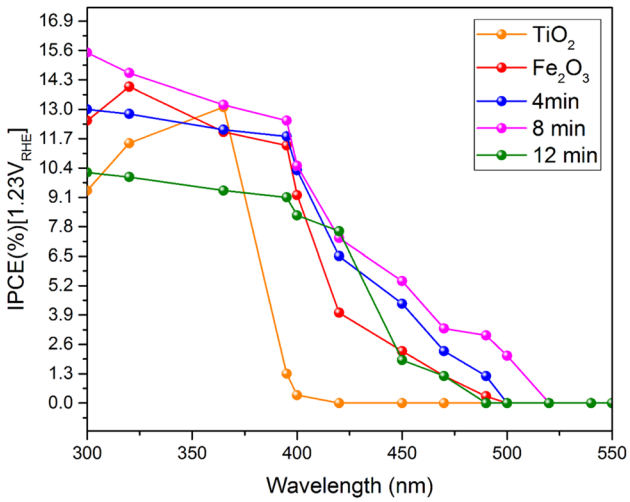

Fig. 10 Incident-photon-to-current efficiency (IPCE) of TiO_2, Fe_2O_3, and TiO_2/Fe_2O_3 films.

substrate, exhibits a type-II staggered band alignment in the 1.0 M NaOH electrolyte (pH 14). This specific alignment is critical for efficient charge separation and is depicted in the energy diagram. Upon illumination, both semiconductors absorb photons and generate electron–hole pairs. At the interface, the unique band alignment drives the photogenerated electrons from the higher-energy conduction band of Fe_2O_3 into the lower-energy conduction band of TiO_2. Simultaneously, holes from the higher-energy valence band of TiO_2 transfer to the lower-energy valence band of Fe_2O_3. This spatial separation prevents the recombination of electrons and holes. The electrons that accumulate in the TiO_2 conduction band travel through the external circuit to the Pt counter electrode to facilitate the hydrogen evolution reaction (HER). Meanwhile, the holes accumulated in the Fe_2O_3 valence band migrate to the semiconductor–electrolyte interface to participate in the oxygen evolution reaction (OER), completing the water-splitting process.[57,58]

For all samples, the incident-photon-to-current efficiency (IPCE) at 1.23 V *vs.* RHE was measured as a function of various incident light wavelengths to compare the behavior of TiO_2 films with Fe_2O_3 and TiO_2/Fe_2O_3 films. The results are presented in Fig. 10. The TiO_2/Fe_2O_3 samples showed enhanced IPCE values compared to pure Fe_2O_3 across the wavelength range of 300–550 nm, especially in the visible region. For instance, the IPCE of TiO_2/Fe_2O_3 (8 min) at 420 nm increased to 7.47%, up from 3.9% for Fe_2O_3 alone. A similar improvement was observed for TiO_2/Fe_2O_3 (4 min), which reached 6.5%. In the UV region, IPCE values for TiO_2/Fe_2O_3 (4 min) were comparable to pure Fe_2O_3, while the values for TiO_2/Fe_2O_3 (12 min) decreased. Notably, at 500 nm, the IPCE of Fe_2O_3 dropped to zero, whereas TiO_2/Fe_2O_3 (8 min) maintained an IPCE value of 1.95% at this wavelength.

These results align with previous studies, which have reported a greater increase in IPCE values in the visible region compared to the UV region.[59] In contrast, studies on Zr, Sn, and Ti doping show that these elements have a minimal impact on the IPCE values of hematite in the visible region but a significant effect in the UV region.[25,30,60]

Mott–Schottky (M–S) calculations were employed to determine the flat band potential (V_{fb}) and donor density (N_d) of Fe_2O_3, TiO_2, and TiO_2/Fe_2O_3 samples. Measurements were taken in the dark at a frequency of 1 kHz, using the equation:

$$\frac{1}{C^2} = \frac{2}{\varepsilon\varepsilon_0 e N_d A^2}\left(E - V_{fb} - \frac{k_B T}{e}\right) \quad (1)$$

where A is the active area, e is electron charge, ε_0 is the permittivity of a vacuum, ε is the dielectric constant, T is the absolute temperature, k is the Boltzmann constant and E is the applied potential.[61,62] The results are shown in Fig. 11.

All films exhibited a positive gradient, confirming that Fe_2O_3, TiO_2, and TiO_2/Fe_2O_3 are n-type semiconductors. As shown in Fig. 11a, the Fe_2O_3 films have a flat band potential around 0.48 V_{RHE} and a donor density of approximately 3.27×10^{19} cm^{-3}. The TiO_2 thin films display a V_{fb} of about 0.16 V *vs.* RHE and a donor density of 1.68×10^{18} cm^{-3}, as seen in Fig. 11b. Fig. 11a also shows that TiO_2/Fe_2O_3 films (4, 8, and 12 min) exhibit V_{fb} values of approximately 0.06, 0.52, and 0.74 V_{RHE}, with corresponding donor densities of 2.24×10^{19}, 4.66×10^{19}, and 1.75×10^{19} cm^{-3}, respectively. The shift in the V_{fb} values for TiO_2/Fe_2O_3 films could be attributed to efficient hole transport from hematite to TiO_2, leading to enhanced water oxidation reactions at the surface.[59] However, since the V_{fb} of Fe_2O_3 typically ranges between 0.4 and 0.8 V_{RHE}, our results for Fe_2O_3 are generally consistent with those reported by Dotan *et al.*[63]

The photoconversion efficiencies of the various photoanodes were assessed using the applied bias photon-to-current conversion efficiency (ABPE), derived from the LSV curves. As illustrated in Fig. 12a, the α-Fe_2O_3 photoanode exhibits a maximum ABPE of only 0.1% at 0.86 V *versus* RHE. The photoanodes prepared for 4 and 12 minutes show ABPE peaks of 0.19% (at 0.9 V *vs.* RHE) and 0.04% (at 1.0 V *vs.* RHE),

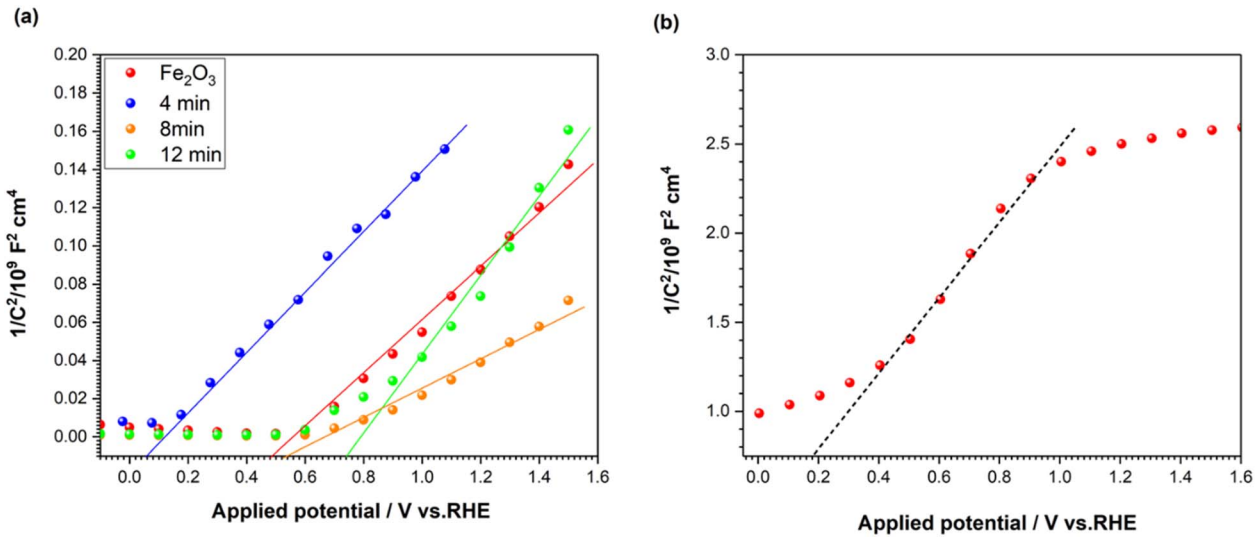

Fig. 11 Mott–Schottky plots for three electrodes: (a) Fe_2O_3 and TiO_2/α-Fe_2O_3 films, and (b) anatase TiO_2 as the photoanode. The flat band potential and donor density of the samples were determined from this analysis.

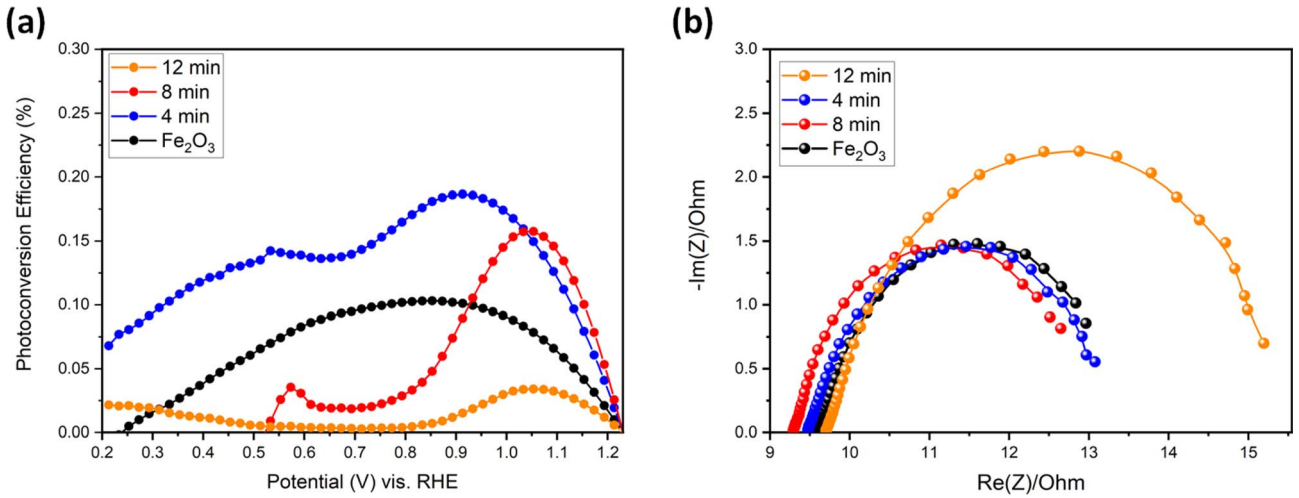

Fig. 12 (a) Applied bias photon-to-current efficiency (ABPE) curves for α-Fe_2O_3 and TiO_2/α-Fe_2O_3 with varying deposition times (4, 8, and 12 minutes). (b) Electrochemical impedance spectroscopy (EIS) for all samples in 1.0 M NaOH electrolyte.

respectively. Notably, the 8-minute photoanode displays a ABPE peak of 0.16% near 1.1 V *vs.* RHE, surpassing that of the bare α-Fe_2O_3 and occurring at a more practically relevant bias for PEC applications.

However, the electrochemical impedance spectroscopy (EIS) measurements provide clear insight into the influence of coating duration on the interfacial charge transfer properties of the photoanodes. The Nyquist plots, which represent the imaginary and real components of the EIS plots (Z' *versus* $-Z''$), were measured at 1.23 V_{RHE} under simulated sunlight conditions (AM 1.5G, 100 mW cm^{-2}) (Fig. 12b). The bare Fe_2O_3 electrode exhibits a semicircle with moderate diameter, reflecting relatively high charge transfer resistance (R_{ct}) due to its intrinsically poor conductivity and high recombination rates. Upon coating for 4 min, the semicircle diameter decreases slightly, suggesting reduced interfacial resistance and improved charge transfer kinetics, likely due to the formation of a thin layer that facilitates more efficient electron transport. The 8 min coated sample shows a comparable semicircle to Fe_2O_3, indicating only moderate improvement, as increased thickness can introduce additional scattering centers or recombination pathways. In contrast, the 12 min coated sample displays the largest semicircle, corresponding to the highest R_{ct}, which can be attributed to excessive coating thickness that hinders charge mobility, blocks active sites, and limits effective interaction with the electrolyte.

6.1. Long-term stability

The stability of photoelectrodes is crucial for the generation and commercial viability of PEC hydrogen production devices. As a result, enhancing the stability of semiconductors has been a focus of recent research. Fig. 13 illustrates the stability of hematite and TiO_2/α-Fe_2O_3 (8 min) films under simulated sunlight at an intensity of 100 mW cm^{-2}. The Fe_2O_3 film, deposited *via* AACVD, remained stable for over 6.5 hours, the photocurrent response measured at 1.0 V *vs.* RHE. Remarkably,

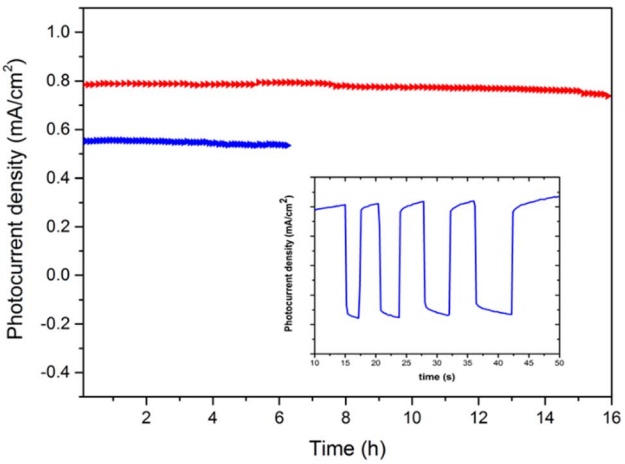

Fig. 13 Polarization curves of the Fe_2O_3 films (blue) and TiO_2/α-Fe_2O_3 films (red) recorded under simulated solar illumination (100 mW cm^{-2}) with a fixed bias of 1 mA cm^{-2}. The measurements were conducted in a 1.0 M NaOH electrolyte under sunlight.

the incorporation of a TiO_2 layer improved the stability of the α-Fe_2O_3 film, extending its performance to over 16 hours.

The morphology of the TiO_2/α-Fe_2O_3 (8 min) film was analyzed using SEM before and after PEC and stability tests. As shown in Fig. 14, the initial morphology featured densely packed particles approximately 500 nm in width (Fig. 14a). However, after undergoing prolonged testing (over 16 hours), the structure transformed into irregular shapes with visible pinholes, voids, and cracks (Fig. 14b). These morphological changes suggest that the sample's stability is influenced by the TiO_2 surface, as TiO_2 exhibits greater stability compared to Fe_2O_3.

Fig. 15 presents the XPS analysis of the TiO_2/α-Fe_2O_3 (8 min) sample before and after stability tests. The results reveal a reduction in XPS intensity for Ti 2p and Fe 2p following the

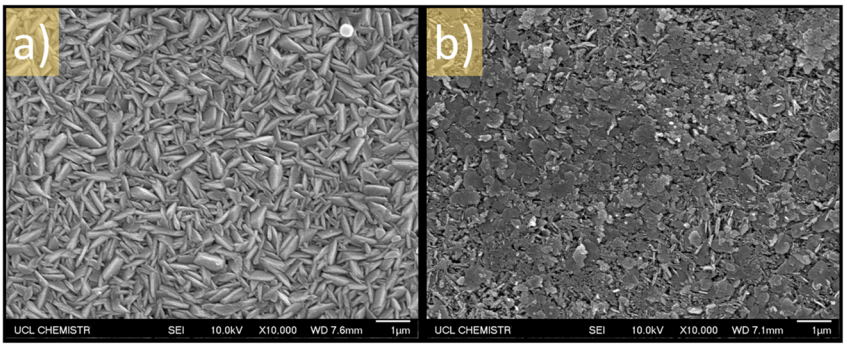

Fig. 14 SEM images of the TiO_2/α-Fe_2O_3 (8 min) anode captured (a) before and (b) after stability tests. The photocurrent stability test was conducted for over 16 hours under simulated solar illumination (100 mW cm^{-2}) with a constant bias of 1.0 mA cm^{-2}.

test, indicating that both TiO_2 and α-Fe_2O_3 underwent decomposition.

7. Transient absorption spectroscopy (TAS)

Transient absorption spectroscopy (TAS) was employed to study the charge carrier dynamics in TiO_2, α-Fe_2O_3, and TiO_2/Fe_2O_3 films over a nanosecond to microsecond timescale at room temperature (25 °C). Previous studies have demonstrated that varying the thickness of TiO_2 on α-Fe_2O_3 enhances photocurrent generation in water-splitting reactions. In this work, TAS was utilized to examine how coupling hematite with TiO_2 influences the dynamics and lifetime of photo-generated charge carriers. Fig. 16 presents the transient absorption spectra of TiO_2, Fe_2O_3, and TiO_2/α-Fe_2O_3 samples. Pristine TiO_2 films exhibit a broad and structured photo-induced absorption (PIA) band with peaks at 630 and 770 nm, aligning with previously reported findings.[64] As reported by Akihiro Furube *et al.*,[64] the broad PIA band comprises multiple components: the 630 nm PIA band is primarily associated with trapped holes, while the 770 nm PIA band corresponds to trapped electrons. Our findings confirm that photogenerated hole absorption occurs around 630 nm, though other studies have suggested a spectral range of 450–570 nm with a lifetime spanning microseconds to milliseconds. However, this interpretation remains a topic of ongoing discussion.[64] The transient absorption data also reveal that the 770 nm PIA band disappears after 100 ns, whereas the 630 nm PIA band remains even beyond 1 μs. This indicates that the electrons have a shorter lifespan than the holes. The TA spectra of Fe_2O_3 sample exhibited an absorption peak at 560 nm, accompanied by a slight tail at 680 nm. This could be linked to trapped photo-generated holes and electrons, or potentially result from reactive oxygen species on the surface.[65–67] Moreover, the signal intensity of pure hematite is twice that of pure TiO_2, as shown in Fig. 16. The behavior of photo-generated holes in TiO_2 and Fe_2O_3 has been studied before using different hole scavengers, such as methanol for TiO_2, and thiocyanate, isopropanol, and iodide for Fe_2O_3.[67,68] The decay dynamics of photo-generated holes in Fe_2O_3 showed no dependence on the chemical environment when measured with

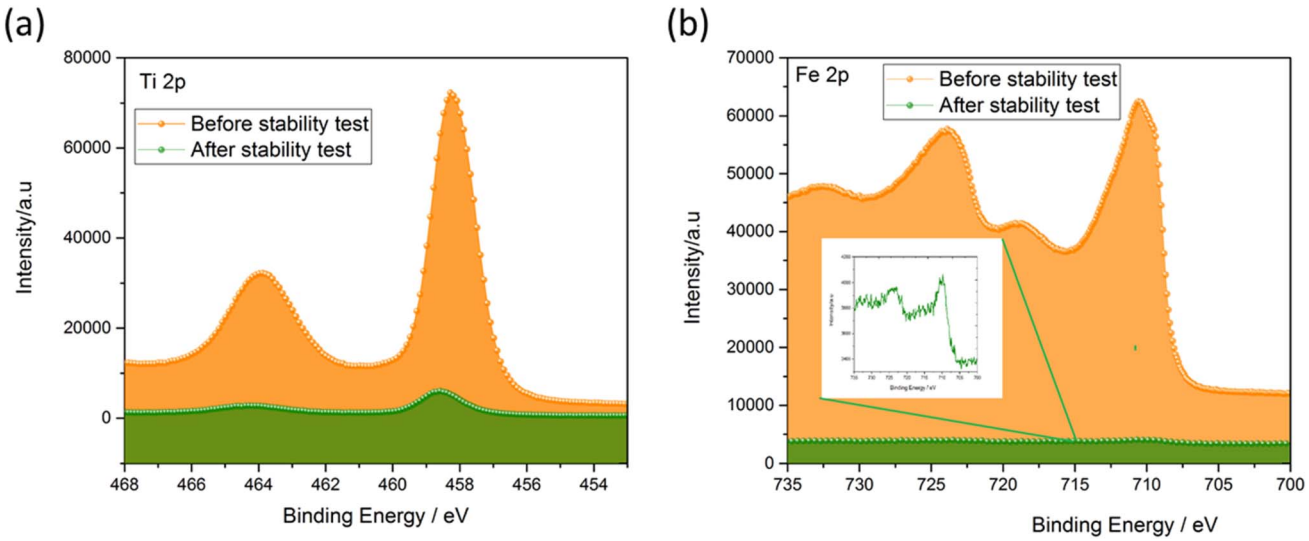

Fig. 15 X-ray photoelectron spectroscopy (XPS) analysis of the surface for (a) Ti 2p and (b) Fe 2p, conducted before and after the stability test.

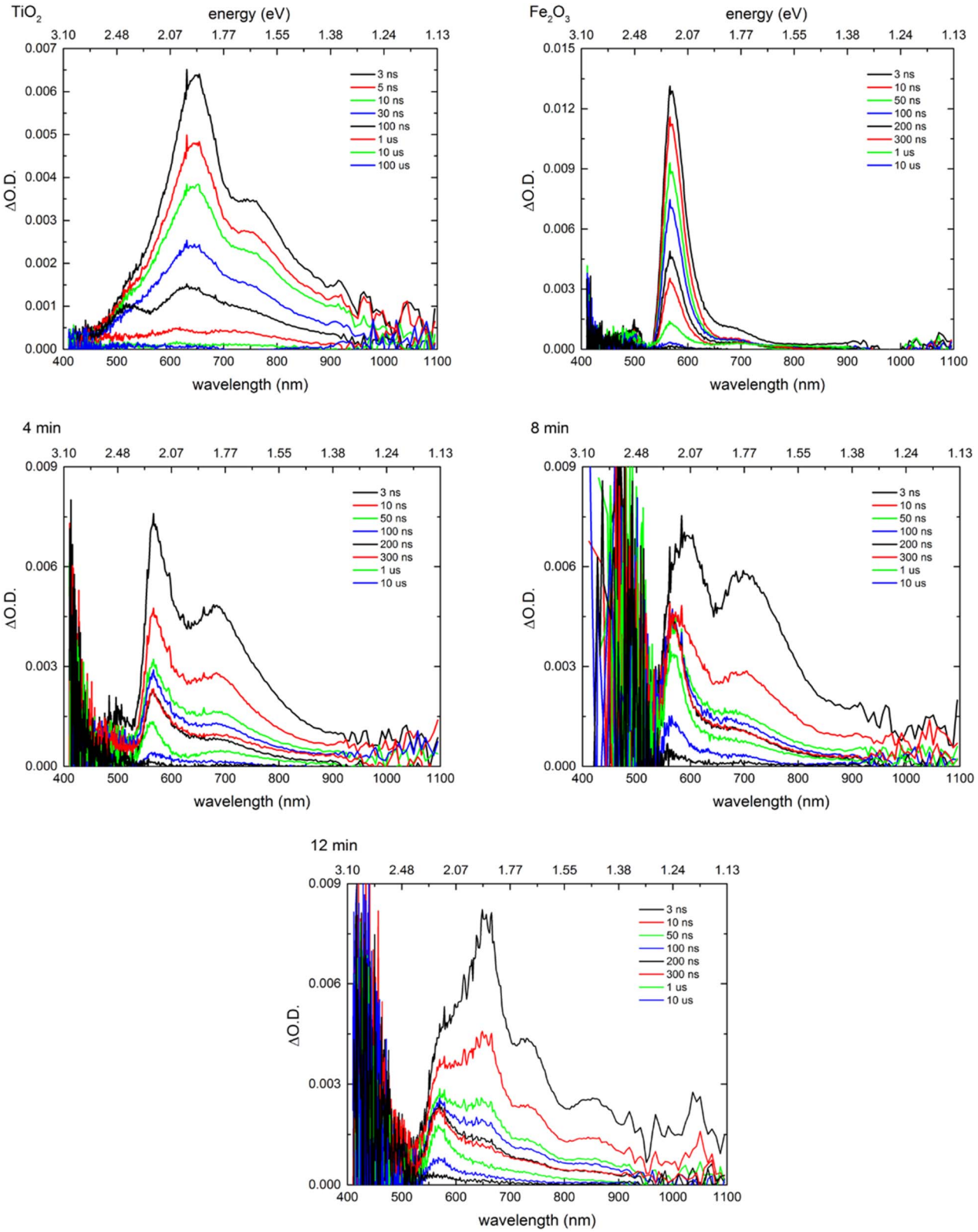

Fig. 16 Transient absorption spectra at various delay times for pure TiO_2, pure Fe_2O_3, and TiO_2/Fe_2O_3 thin films. The pump wavelength is 355 nm, with a fluence density of 300 μJ cm^{-2}.

TAS at 580 nm over a time scale of μs–ms. In contrast, the decay dynamics of photo-generated holes in TiO_2 exhibited a significant sensitivity to methanol at 460 nm.[68]

In our experiments, the TiO_2/Fe_2O_3 samples exhibit absorption at 560 and 700 nm, which we attribute to trapped photogenerated holes in Fe_2O_3, as the holes in Fe_2O_3 absorb

significantly more strongly than those in TiO_2. This may cause a spectral overlap of trapped holes in Fe_2O_3 with those in TiO_2. However, when the TiO_2 thickness is increased (as in the 12-minute sample), absorption bands at 560 and 650 nm are observed for Fe_2O_3 and TiO_2, respectively, along with a band at 770 nm for electrons.

The TA spectra of the series of TiO_2/Fe_2O_3 films illustrate how the spectra change as the TiO_2 layer thickness increases

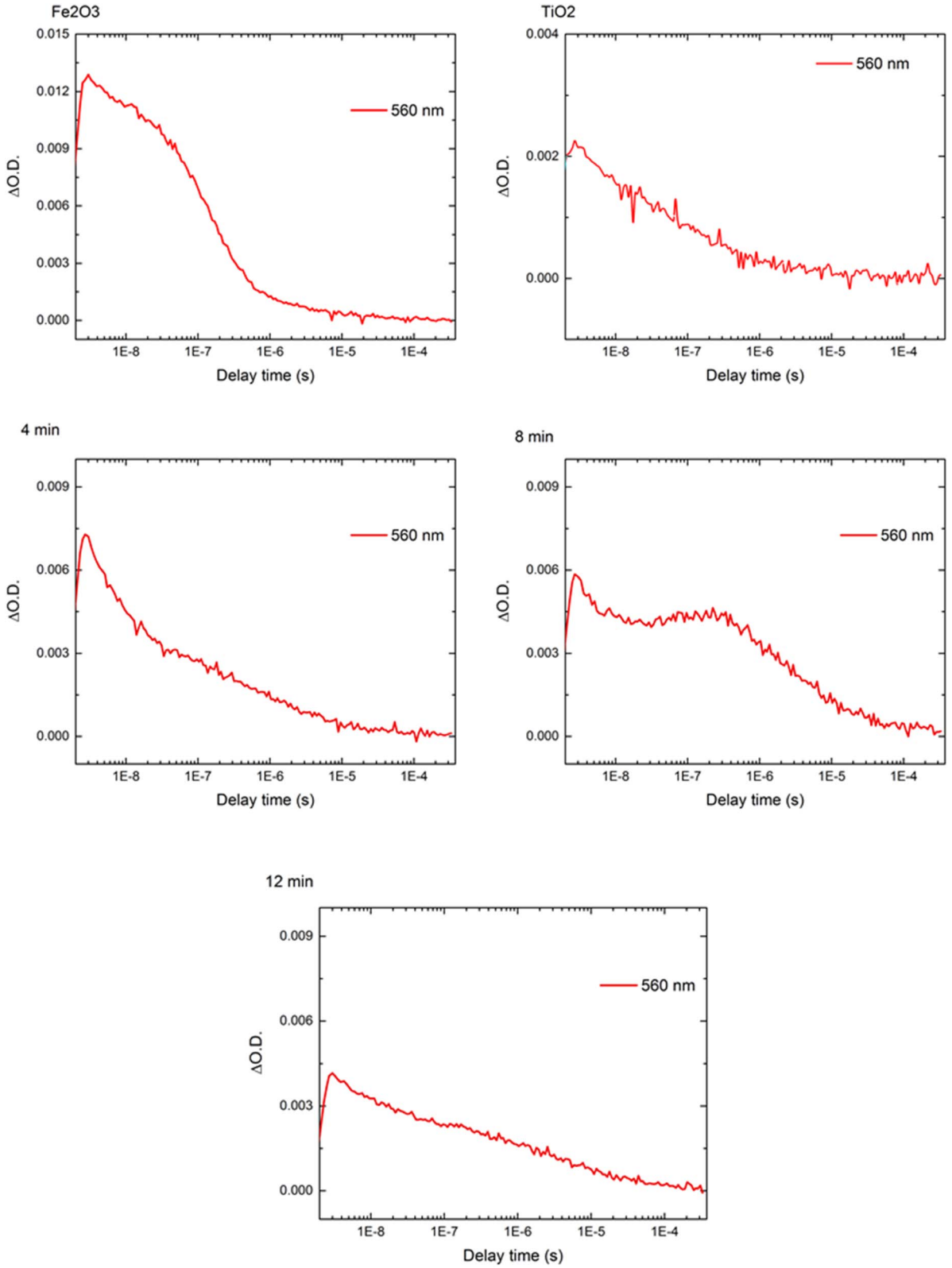

Fig. 17 Transient absorption decay profiles at 560 nm for pure TiO_2, pure Fe_2O_3, and TiO_2/Fe_2O_3 thin films.

(*i.e.*, with longer reaction times). For the thinnest TiO_2 layer, the TA spectra show a larger contribution from Fe_2O_3, with a prominent PIA band peaking around 560 nm. As the TiO_2 layer thickness grows, the contribution from TiO_2 gradually increases, and the 650 nm PIA band becomes more prominent than the 560 nm PIA band.

The temporal evolution of the transient absorption decay was measured at 560 nm for TiO_2 excited at 355 nm with pulse energy densities of 300 μJ cm^{-2} in the sub-nanosecond range. For TiO_2, the fastest TA decay occurred at 560 nm with a lifetime of $t_{50\%} = 85$ ns, where $t_{50\%}$ represents the time for the signal to decay to 50% of its initial amplitude. For hematite, the TA decay at 560 nm showed an initial signal intensity of about 0.013 ΔO.D. with a lifetime of $t_{50\%} = 112$ ns. The TiO_2/α-Fe_2O_3 (4, 8, 12 min) samples exhibited initial signal intensities of 0.075, 0.006, and 0.0045 ΔO.D. at 560 nm, respectively, with lifetimes of $t_{50\%}$ = 66 ns, 1200 ns, and 880 ns. Notably, the TiO_2/α-Fe_2O_3 (8 min) sample showed slower decays and a significant increase in signal intensity at 560 nm compared to pure Fe_2O_3 and TiO_2. These findings align with the photocurrent data obtained during water oxidation (Fig. 17), suggesting that the low efficiency of pure Fe_2O_3 is due to rapid electron–hole recombination. However, at 560 nm, single-layer TiO_2 shows a lower signal intensity than Fe_2O_3 because the valence band of Fe_2O_3 is higher than that of TiO_2. In contrast, TiO_2/Fe_2O_3 films, particularly the TiO_2/α-Fe_2O_3 (8 min) sample, exhibit much slower recombination, which could be attributed to the transfer of photogenerated holes from Fe_2O_3 to TiO_2. Additionally, photogenerated electrons in TiO_2 may be transferred to Fe_2O_3, extending the photo hole lifetime in the TiO_2 films.

8. Conclusion

Fe_2O_3 film was deposited on FTO glass using aerosol-assisted chemical vapor deposition (AACVD) at 450 °C, employing iron(II) acetylacetonate [$Fe(CH_3COCH{=}C(O)CH_3)_2$] as the precursor. Subsequently, titanium isopropoxide [$Ti(OCH(CH_3)_2)_4$] was used in atmospheric pressure chemical vapor deposition (APCVD) to deposit TiO_2 on the Fe_2O_3 films, with deposition times of 4, 8, and 12 minutes. XRD and Raman spectroscopy confirmed the phase formation of the resulting samples, with Fe_2O_3 and TiO_2 present only in the hematite and anatase phases, respectively. XPS studies indicated that Fe and Ti were in the Fe^{3+} and Ti^{4+} oxidation states. The bandgap of TiO_2/Fe_2O_3 films was found to be smaller than that of Fe_2O_3 films, and a significant increase in photocurrent was observed in TiO_2/Fe_2O_3 films compared to pure Fe_2O_3 or TiO_2 films. PEC measurements of TiO_2/Fe_2O_3 films deposited on FTO showed a photocurrent of 1.7 mA cm^{-2} at 1.23 V *vs.* NHE in 1.0 M NaOH, under AM 1.5 sunlight conditions. Transient absorption spectroscopy (TAS) revealed that TiO_2/Fe_2O_3 had a longer lifetime compared to pure hematite, which could be due to reduced electron–hole recombination, contributing to the improved photocurrent.

This study highlights the potential of TiO_2/Fe_2O_3 films as a promising material for water splitting with high stability.

Conflicts of interest

There are no conflicts to declare.

Data availability

Additional datasets available upon reasonable request.

The supporting data are available within the article and its SI. See DOI: **https://doi.org/10.1039/d5ra05064b**.

References

1 C. Bailleux, *Int. J. Hydrogen Energy*, 1981, **6**, 461–471.
2 A. Landman, H. Dotan, G. E. Shter, M. Wullenkord, A. Houaijia, A. Maljusch, G. S. Grader and A. Rothschild, *Nat. Mater.*, 2017, **16**, 646–651.
3 C.-H. Liao, C.-W. Huang and J. C. S. Wu, *Catalysts*, 2012, **2**, 490–516.
4 K. Mazloomi and C. Gomes, *Renewable Sustainable Energy Rev.*, 2012, **16**, 3024–3033.
5 S. J. A. Moniz, S. A. Shevlin, D. J. Martin, Z.-X. Guo and J. Tang, *Energy Environ. Sci.*, 2015, **8**, 731–759.
6 R. di Primio, B. Horsfield and M. A. Guzman-Vega, *Nature*, 2000, **406**, 173–176.
7 N. S. Lewis and D. G. Nocera, *Proc. Natl. Acad. Sci. U. S. A.*, 2006, **103**, 15729–15735.
8 S. Solomon, G.-K. Plattner, R. Knutti and P. Friedlingstein, *Proc. Natl. Acad. Sci. U. S. A.*, 2009, **106**, 1704–1709.
9 A. Fujishima and K. Honda, *Nature*, 1972, **238**, 37–38.
10 A. M. Alotaibi, S. Sathasivam and I. P. Parkin, *RSC Adv.*, 2015, **5**, 67944–67950.
11 A. M. Alotaibi, B. A. D. Williamson, S. Sathasivam, A. Kafizas, M. Alqahtani, C. Sotelo-Vazquez, J. Buckeridge, J. Wu, S. P. Nair, D. O. Scanlon and I. P. Parkin, *ACS Appl. Mater. Interfaces*, 2020, **12**, 15348–15361.
12 M. Andersson, L. Österlund, S. Ljungström and A. Palmqvist, *J. Phys. Chem. B*, 2002, **106**, 10674–10679.
13 M. P. Dare-Edwards, J. B. Goodenough, A. Hamnett and P. R. Trevellick, *J. Chem. Soc., Faraday Trans. 1*, 1983, **79**, 2027–2041.
14 J.-W. Jang, C. Du, Y. Ye, Y. Lin, X. Yao, J. Thorne, E. Liu, G. McMahon, J. Zhu, A. Javey, J. Guo and D. Wang, *Nat. Commun.*, 2015, **6**, 7447.
15 A. Kay, I. Cesar and M. Grätzel, *J. Am. Chem. Soc.*, 2006, **128**, 15714–15721.
16 K. G. McGregor, M. Calvin and J. W. Otvos, *J. Appl. Phys.*, 1979, **50**, 369–373.
17 C. Sanchez, K. D. Sieber and G. A. Somorjai, *J. Electroanal. Chem. Interfacial Electrochem.*, 1988, **252**, 269–290.
18 R. Shinar and J. H. Kennedy, *Sol. Energy Mater.*, 1982, **6**, 323–335.
19 K. Sivula, F. L. Formal and M. Grätzel, *Chem. Mater.*, 2009, **21**, 2862–2867.
20 J. H. Kennedy and K. W. Frese, *J. Electrochem. Soc.*, 1978, **125**, 709.
21 I. Balberg and H. L. Pinch, *J. Magn. Magn. Mater.*, 1978, **7**, 12–15.

22 A. B. Murphy, P. R. F. Barnes, L. K. Randeniya, I. C. Plumb, I. E. Grey, M. D. Horne and J. A. Glasscock, *Int. J. Hydrogen Energy*, 2006, **31**, 1999–2017.
23 J. Deng, J. Zhong, A. Pu, D. Zhang, M. Li, X. Sun and S.-T. Lee, *J. Appl. Phys.*, 2012, **112**, 084312.
24 M. Forster, R. J. Potter, Y. Yang, Y. Li and A. J. Cowan, *ChemPhotoChem*, 2018, **2**, 183–189.
25 Y. Ling, G. Wang, D. A. Wheeler, J. Z. Zhang and Y. Li, *Nano Lett.*, 2011, **11**, 2119–2125.
26 A. Pu, J. Deng, M. Li, J. Gao, H. Zhang, Y. Hao, J. Zhong and X. Sun, *J. Mater. Chem. A*, 2014, **2**, 2491–2497.
27 T. Wang, W. Luo, X. Wen, Z. Zou and W. Huang, *ChemNanoMat*, 2016, **2**, 652–655.
28 K. L. Hardee and A. J. Bard, *J. Electrochem. Soc.*, 1975, **122**, 739.
29 R. K. Quinn, R. D. Nasby and R. J. Baughman, *Mater. Res. Bull.*, 1976, **11**, 1011–1017.
30 S. Shen, P. Guo, D. A. Wheeler, J. Jiang, S. A. Lindley, C. X. Kronawitter, J. Z. Zhang, L. Guo and S. S. Mao, *Nanoscale*, 2013, **5**, 9867–9874.
31 G. Wang, Y. Ling, D. A. Wheeler, K. E. N. George, K. Horsley, C. Heske, J. Z. Zhang and Y. Li, *Nano Lett.*, 2011, **11**, 3503–3509.
32 M. Barroso, C. A. Mesa, S. R. Pendlebury, A. J. Cowan, T. Hisatomi, K. Sivula, M. Grätzel, D. R. Klug and J. R. Durrant, *Proc. Natl. Acad. Sci. U. S. A.*, 2012, **109**, 15640–15645.
33 F. L. Formal, N. Tétreault, M. Cornuz, T. Moehl, M. Grätzel and K. Sivula, *Chem. Sci.*, 2011, **2**, 737–743.
34 L. Xi, P. S. Bassi, S. Y. Chiam, W. F. Mak, P. D. Tran, J. Barber, J. S. C. Loo and L. H. Wong, *Nanoscale*, 2012, **4**, 4430–4433.
35 V. S. Kumbhar, K. Lee, N. R. Chodankar, A. Al Ghaferi and J.-J. Shim, *Int. J. Hydrogen Energy*, 2025, **142**, 159–167.
36 A. M. Alotaibi, E. Muayqil, N. Al Abass, M. A. Alhajji, A. A. Bubshait, N. E. Alhazmi and A. A. Almuqhim, *Renewable Energy*, 2024, **235**, 121326.
37 C. Nomellini, A. Polo, C. A. Mesa, E. Pastor, G. Marra, I. Grigioni, M. V. Dozzi, S. Giménez and E. Selli, Improved Photoelectrochemical Performance of WO_3/$BiVO_4$ Heterojunction Photoanodes via WO_3 Nanostructuring, *ACS Appl. Mater. Interfaces*, 2023, **15**, 52436–52447.
38 R. Han, W. Li, W. Pan, M. Zhu, D. Zhou and F. Li, *Sci. Rep.*, 2014, **4**, 7493.
39 Q. Wei, Z. Li, Z. Zhang and Q. Zhou, *Mater. Trans.*, 2009, **50**, 1351–1354.
40 S. Ponja, S. Sathasivam, N. Chadwick, A. Kafizas, S. M. Bawaked, A. Y. Obaid, S. Al-Thabaiti, S. N. Basahel, I. P. Parkin and C. J. Carmalt, *J. Mater. Chem. A*, 2013, **1**, 6271–6278.
41 J. Tauc, *Mater. Res. Bull.*, 1968, **3**, 37–46.
42 A. Furlani, M. V. Russo, G. Polzonetti, K. Martin, H. H. Wang and J. R. Ferraro, *Appl. Spectrosc.*, 1990, **44**, 331–334.
43 R. P. Gupta and S. K. Sen, *Phys. Rev. B: Solid State*, 1974, **10**, 71–77.
44 R. P. Gupta and S. K. Sen, *Phys. Rev. B: Solid State*, 1975, **12**, 15–19.
45 A. P. Grosvenor, B. A. Kobe, M. C. Biesinger and N. S. McIntyre, *Surf. Interface Anal.*, 2004, **36**, 1564–1574.
46 N. S. McIntyre and D. G. Zetaruk, *Anal. Chem.*, 1977, **49**, 1521–1529.
47 K. Gajda-Schrantz, S. Tymen, F. Boudoire, R. Toth, D. K. Bora, W. Calvet, M. Grätzel, E. C. Constable and A. Braun, *Phys. Chem. Chem. Phys.*, 2013, **15**, 1443–1451.
48 A. P. Singh, N. Kodan, B. R. Mehta, A. Dey and S. Krishnamurthy, *Mater. Res. Bull.*, 2016, **76**, 284–291.
49 X. Guo, L. Wang and Y. Tan, *Nano Energy*, 2015, **16**, 320–328.
50 H. Lu, S. Fang, J. Hu, B. Chen, R. Zhao, H. Li, C. M. Li and J. Ye, *ACS Omega*, 2020, **5**, 19861–19867.
51 Y. Sun, L. Zhang, X. Zhou, Y. Ji, Y. Zhu, Q. Fu, X. Chen, X. Cheng and W. Yan, *New J. Chem.*, 2025, **49**, 10869–10878.
52 N. Dai, Y. Zhang, Z. Peng and J. Liu, *J. Alloys Compd.*, 2025, **1018**, 179294.
53 A. Memar, C. M. Phan and M. O. Tade, *Int. J. Hydrogen Energy*, 2015, **40**, 8642–8649.
54 L. Xia, J. Bai, J. Li, Q. Zeng, X. Li and B. Zhou, *Appl. Catal., B*, 2016, **183**, 224–230.
55 P. I. Kyesmen, N. Nombona and M. Diale, *J. Alloys Compd.*, 2021, **863**, 158724.
56 Y.-K. Hsu, Y.-C. Chen and Y.-G. Lin, *ACS Appl. Mater. Interfaces*, 2015, **7**, 14157–14162.
57 B. Singh, S. Gautam, G. C. Behera, R. Kumar, V. Aggarwal, J. S. Tawale, R. Ganesan, S. C. Roy and S. S. Kushvaha, *Nano Express*, 2024, **5**, 015006.
58 B. Singh, G. C. Behera, B. K. Pradhan, S. Gautam, V. Aggarwal, R. Kumar, M. S. Kumar, R. Ganesan, S. C. Roy and S. S. Kushvaha, *J. Mater. Sci.*, 2024, **59**, 15201–15220.
59 S. Shen, J. Zhou, C.-L. Dong, Y. Hu, E. N. Tseng, P. Guo, L. Guo and S. S. Mao, *Sci. Rep.*, 2014, **4**, 6627.
60 S. Shen, C. X. Kronawitter, D. A. Wheeler, P. Guo, S. A. Lindley, J. Jiang, J. Z. Zhang, L. Guo and S. S. Mao, *J. Mater. Chem. A*, 2013, **1**, 14498–14506.
61 C. H. Bak, K. Kim, K. Jung, J.-B. Kim and J.-H. Jang, *J. Mater. Chem. A*, 2014, **2**, 17249–17252.
62 B. Iandolo, H. Zhang, B. Wickman, I. Zorić, G. Conibeer and A. Hellman, *RSC Adv.*, 2015, **5**, 61021–61030.
63 H. Dotan, K. Sivula, M. Grätzel, A. Rothschild and S. C. Warren, *Energy Environ. Sci.*, 2011, **4**, 958–964.
64 R. Katoh, M. Murai and A. Furube, *Chem. Phys. Lett.*, 2010, **500**, 309–312.
65 Z. Huang, Y. Lin, X. Xiang, W. Rodríguez-Córdoba, K. J. McDonald, K. S. Hagen, K.-S. Choi, B. S. Brunschwig, D. G. Musaev, C. L. Hill, D. Wang and T. Lian, *Energy Environ. Sci.*, 2012, **5**, 8923–8926.
66 G. X. Pei, J. H. J. Wijten and B. M. Weckhuysen, *Phys. Chem. Chem. Phys.*, 2018, **20**, 9806–9811.
67 S. R. Pendlebury, M. Barroso, A. J. Cowan, K. Sivula, J. Tang, M. Grätzel, D. Klug and J. R. Durrant, *Chem. Commun.*, 2011, **47**, 716–718.
68 J. Tang, J. R. Durrant and D. R. Klug, *J. Am. Chem. Soc.*, 2008, **130**, 13885–13891.